Check for updates

Research Article | Vol. 30, No. 20 / 26 Sep 2022 / Optics Express 36176

Optics EXPRESS

Scheme to estimate water-leaving albedo from remotely sensed chlorophyll-a concentration

XIAOLONG YU* AND ZHONGPING LEE

State Key Lab of Marine Environmental Science, College of Ocean and Earth Sciences, Xiamen University, Xiamen 361005, China

*xlyu@xmu.edu.cn

Abstract: Water-leaving albedo ($\alpha_w(\lambda)$) is an important component of the ocean surface albedo and is conventionally estimated based on remotely sensed chlorophyll-a concentration (Chl) (termed Chl-α_w). We show that estimated $\alpha_w(\lambda)$ by Chl-α_w could be significantly biased in global oceans, because there is no guarantee of closure between the modeled remote sensing reflectance ($R_{rs}(\lambda)$) from Chl-inferred inherent optical properties (IOPs) and the input $R_{rs}(\lambda)$ that is used to derive Chl. We thus propose a simple and improved scheme, termed Chl-α_w_new, and show that the step to infer IOPs from Chl is not necessary, where $\alpha_w(\lambda)$ can be accurately estimated from satellite-measured $R_{rs}(\lambda)$ and a Chl-based look-up-table (LUT) for the bidirectional relationships of angular $R_{rs}(\lambda)$. Evaluations with both HydroLight simulations and satellite measurements show that Chl-α_w_new is equivalent to the recently developed α_w scheme based on IOPs (IOPs-α_w, [Remote Sens. Environ. 269, 112807]), where both schemes could significantly improve the estimation of $\alpha_w(\lambda)$ compared to Chl-α_w. Comparisons among Chl-α_w, Chl-α_w_new, and IOPs-α_w highlight that optical closure of $R_{rs}(\lambda)$ is essential for accurate remote sensing of $\alpha_w(\lambda)$, while the model for $R_{rs}(\lambda)$ bidirectionality has rather minor impacts. The impact of improved $\alpha_w(\lambda)$ estimations on the solar flux exchanges at the air-sea interface is preliminarily evaluated in this effort, where the use of Chl-α_w_new could increase the estimation of reflected solar radiation by over 68.7% in turbid waters compared to that using Chl-α_w, highlighting the necessity of incorporating accurate α_w schemes into the coupled ocean-atmosphere models, especially for regional models in coastal oceans.

1. Introduction

The broadband ocean surface albedo (α) is a key parameter in the coupled ocean-atmosphere models to quantify the amount of solar energy absorbed by the ocean and that reflected into the atmosphere [1]. α can be computed from the spectral ocean surface albedo $\alpha(\lambda)$ over the full shortwave domain, with $\alpha(\lambda)$ calculated as the ratio of spectral upward irradiance $E_u(0^+, \lambda)$ (in W m^{-2} nm^{-1}) to spectral downward irradiance $E_d(0^+, \lambda)$ just above the sea surface [2]. In general, $\alpha(\lambda)$ is contributed by both surface-reflected and water-leaving radiation [3,4], where the surface-reflected albedo has been extensively investigated since the 1950s and is conventionally parameterized as a function of solar zenith angle and wind speed. The surface-reflected albedo is also slightly dependent on the atmospheric properties, such as aerosol optical thickness [5–8]. The water-leaving albedo, termed $\alpha_w(\lambda)$ and defined as the ratio of water-leaving irradiance $E_w(\lambda)$ to $E_d(0^+, \lambda)$, is commonly estimated using the concentration of chlorophyll-a (Chl, in mg/m^3) [9–11].

The basis of the existing α_w scheme, such as the one proposed in Feng et al. [10], is that $E_w(\lambda)$, by definition, is the integral of water-leaving radiance ($L_w(\lambda)$, in W m^{-2} nm^{-1} sr^{-1}) in the upper hemisphere above the sea surface, weighted by the cosine of viewing zenith angle [12].

#469201 https://doi.org/10.1364/OE.469201
Journal © 2022 Received 29 Jun 2022; revised 3 Sep 2022; accepted 8 Sep 2022; published 19 Sep 2022

Optics EXPRESS

Thus, $\alpha_{\mathrm{w}}(\lambda)$ can be expressed as

$$\alpha_{\mathrm{w}}(\lambda,\theta_s)=\frac{E_{\mathrm{w}}(\lambda,\theta_s)}{E_{\mathrm{d}}(0^+,\lambda,\theta_s)}=\frac{\int_0^{2\pi}\int_0^{\pi/2}L_{\mathrm{w}}(\lambda,\theta_s,\theta_v,\varphi)\cos\theta_v\sin\theta_v d\theta_v d\varphi}{E_{\mathrm{d}}(0^+,\lambda,\theta_s)},\tag{1}$$

where θ_{s}, θ_{v}, and φ are the solar zenith, viewing zenith, and viewing azimuth angles, describing the angular geometry of $L_{\mathrm{w}}(\lambda)$ in the upper hemisphere. The three angles are collectively termed as Ω in the following for brevity. Given that the ratio of $L_{\mathrm{w}}(\lambda)$ to $E_{\mathrm{d}}(0^+, \lambda)$ is defined as the remote sensing reflectance $R_{\mathrm{rs}}(\lambda)$ (in sr^{-1}), $\alpha_{\mathrm{w}}(\lambda)$ can thus be calculated as the integral of angular $R_{\mathrm{rs}}(\lambda, \Omega)$

$$\alpha_{\mathrm{w}}(\lambda,\theta_s)=\int_0^{2\pi}\int_0^{\pi/2}R_{\mathrm{rs}}(\lambda,\theta_s,\theta_v,\varphi)\cos\theta_v\sin\theta_v d\theta_v d\varphi.\tag{2}$$

The angular variation of $R_{\mathrm{rs}}(\lambda, \Omega)$ in Feng et al. [10] is represented by the bidirectional reflectance distribution function (BRDF) developed by Morel and Gentili [13], which is expressed as

$$R_{\mathrm{rs}}(\lambda,\Omega)=\frac{L_{\mathrm{w}}(\lambda,\Omega)}{E_{\mathrm{d}}(0^+,\lambda,\theta_s)}=\Re(\lambda,\theta_s,\theta_v,W)\frac{f(\lambda,\theta_s,Chl)}{Q(\lambda,\theta_s{}',\varphi,Chl)}\frac{b_b(\lambda)}{a(\lambda)}.\tag{3}$$

Here, $\Re$ relates the transmittance of radiance crossing the water-air interface, *f/Q* is the in-water BRDF term, with *f* the model factor linking the irradiance reflectance just beneath the surface (R_0) to inherent optical properties (IOPs) and Q the bidirectional function. $a(\lambda)$ and $b_b(\lambda)$ are the water IOPs, representing the total absorption and backscattering coefficients, respectively. W and $\theta_s{}'$ in Eq. (3) are the wind speed (in m/s) and the refracted solar zenith angle below the sea surface, respectively.

In the implementation of the scheme proposed by Feng et al. [10], $\alpha_{\mathrm{w}}(\lambda)$ can be estimated from Chl following Eqs. (2)–(3). Briefly, $a(\lambda)$ and $b_b(\lambda)$ in Eq. (3) are inferred from Chl following the empirical relationships of Morel and Maritorena [14], with Chl from the standard product from satellite ocean color missions (*e.g.*, the NASA OceanColor web, https://oceancolor.gsfc.nasa.gov). Note that this Chl standard product is derived from satellite-measured $R_{\mathrm{rs}}(\lambda)$ using the empirical Ocean Color Index (OCI) algorithm [15–17]. The values of $\Re$ for specific viewing angles can be extracted from the look-up-table (LUT) provided in Gordon [18], with $\Re$ later corrected for the solar zenith effects following Wang [19]. The values of *f/Q* can be retrieved from a separate LUT provided in Morel et al. [20] for different Chl values and viewing angles. Thus, the angular $R_{\mathrm{rs}}(\lambda)$ can be obtained from Eq. (3), which are then used to estimate $\alpha_{\mathrm{w}}(\lambda)$ via Eq. (2). This scheme is hereafter referred to as Chl-α_{w}.

However, in this process of calculating $R_{\mathrm{rs}}(\lambda, \Omega)$ in the upper hemisphere when employing Chl-α_{w}, Chl is a "middle man", there is no check of closure between the satellite-measured $R_{\mathrm{rs}}(\lambda)$ and the modeled $R_{\mathrm{rs}}(\lambda)$ from the Chl-inferred IOPs via Eq. (3). It is therefore of interest to investigate how this closure issue of $R_{\mathrm{rs}}(\lambda)$ may contribute to the uncertainties of estimated $\alpha_{\mathrm{w}}(\lambda)$ by Chl-α_{w}. Other α_{w} schemes, such as those proposed by Jin et al. [11] and adopted later by Séférian et al. [9], related $\alpha_{\mathrm{w}}(\lambda)$ to the irradiance reflectance just beneath the surface ($R_0(\lambda)$), where $R_0(\lambda)$ is also modeled from Chl using the empirical Chl-IOPs relationship of Morel and Maritorena [14]. Thus, estimated $\alpha_{\mathrm{w}}(\lambda)$ by Jin et al. [11] may also be subject to uncertainties due to no closure of $R_{\mathrm{rs}}(\lambda)$. In this effort, we aim at demonstrating the lack of internal consistency of current Chl-based schemes and proposing an improved scheme that would avoid the closure issue of $R_{\mathrm{rs}}(\lambda)$.

2. Improved Chl-based scheme for α_w

The closure issue of $R_{rs}(\lambda)$ can be simply illustrated by comparing satellite-measured $R_{rs}(\lambda)$ with that modeled from Chl. As a demonstration, the monthly composite $R_{rs}(\lambda)$ product of Visible Infrared Imaging Radiometer Suite (VIIRS) of March 2019 was employed here with descriptions of VIIRS imagery provided in Section 3.2. First, Chl was estimated from VIIRS $R_{rs}(\lambda)$ using the OCI algorithm, from which $R_{rs}(\lambda)$ can be modeled by Chl-inferred IOPs following Eq. (3). Given that VIIRS $R_{rs}(\lambda)$ product is corrected to the nadir-viewed $R_{rs}(\lambda)$ with the Sun at the zenith [18,19], *i.e.*, equivalent to $R_{rs}(\lambda,0,0,0)$, the modeled $R_{rs}(\lambda)$ from Chl is thus computed via Eq. (3) with the values of $\Re$ and f/Q extracted from their respective LUT for $\theta_s = 0$ and $\theta_v = 0$. Then, we calculate the difference between VIIRS-measured $R_{rs}(\lambda,0,0,0)$ and the modeled $R_{rs}(\lambda,0,0,0)$ from Chl. The differences between the two $R_{rs}(\lambda)$, quantified by the relative percentage difference (RPD), in the global ocean are shown in Fig. 1 for the five VIIRS bands in the visible domain (*i.e.*, 410, 443, 486, 551, and 671 nm). RPD is defined as

$$\text{RPD} = (y - x)/x \times 100\%, \tag{4}$$

where x and y are the modeled $R_{rs}(\lambda,0,0,0)$ and VIIRS-measured $R_{rs}(\lambda,0,0,0)$, respectively.

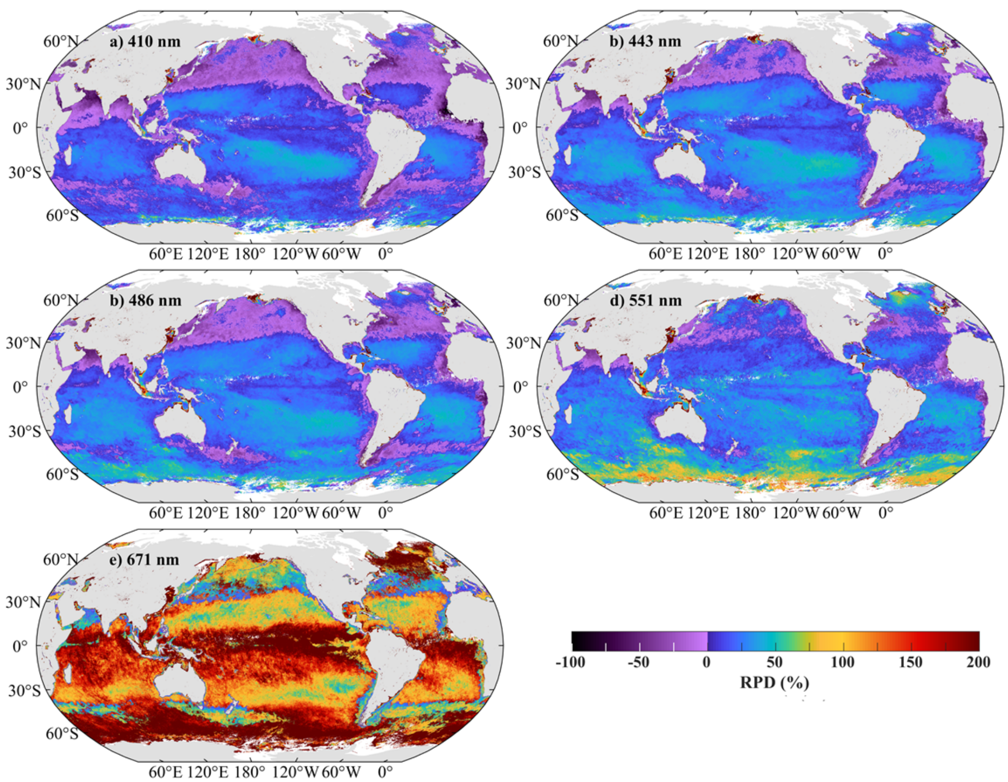

Fig. 1. The relative percentage difference (RPD) of the VIIRS $R_{rs}(\lambda)$ in March 2019, referring to the modeled $R_{rs}(\lambda)$ from Chl-inferred IOPs using Eq. (3).

Results in Fig. 1 suggest that the modeled $R_{rs}(\lambda)$ via the Chl-α_w system significantly deviate from the input, satellite-measured, $R_{rs}(\lambda)$. For example, for 45.6% of the global ocean, the absolute RPD is greater than 25% for $R_{rs}(443)$ (see Fig. 1(b)), while 54.1% of the global ocean is observed with an absolute RPD greater than 25% for $R_{rs}(551)$ (see Fig. 1(d)). These deviations are attributed to the uncertainties in Chl-inferred IOPs, as the validity of the Chl-IOPs relationship of Morel and Maritorena [14] relies heavily on the Chl-specific absorption and Chl-specific backscattering coefficients, which varies greatly in the global ocean [21–25]. In other words, using fixed Chl-IOPs relationships would result in large errors in the derived IOPs in global oceans, and the errors will be propagated to the modeled $R_{\mathrm{rs}}(\lambda)$, and thus the estimated $\alpha_{\mathrm{w}}(\lambda)$.

As indicated by Eq. (2), the key information required for the estimation of $\alpha_{\mathrm{w}}(\lambda)$ is the angular distribution of $R_{\mathrm{rs}}(\lambda)$, whereas satellite ocean color remote sensing provides $R_{\mathrm{rs}}(\lambda)$ for one set of Ω, referred to as $R_{\mathrm{rs}}(\lambda, \Omega_0)$ hereafter. Based on Eq. (3), $R_{\mathrm{rs}}(\lambda, \Omega)$ is related to $R_{\mathrm{rs}}(\lambda, \Omega_0)$ through

$$R_{\mathrm{rs}}(\lambda, \Omega) = R_{\mathrm{rs}}(\lambda, \Omega_0)\frac{\Re(\lambda, \Omega, W)}{\Re(\lambda, \Omega_0, W)}\frac{\Psi(\lambda, \Omega, Chl)}{\Psi(\lambda, \Omega_0, Chl)}, \tag{5}$$

with Ψ for *f/Q*. Since $R_{\mathrm{rs}}(\lambda, \Omega_0)$ is provided by satellite measurement, what is required for the estimation of angular $R_{\mathrm{rs}}(\lambda, \Omega)$ is the ratio of $\Re$ (Ω) to $\Re$ (Ω_0) and the ratio of $\Psi(\Omega)$ to $\Psi(\Omega_0)$ for any given λ and Chl. Thus, it is not necessary to infer IOPs from Chl for the estimation of $\alpha_{\mathrm{w}}(\lambda)$ when $R_{\mathrm{rs}}(\lambda, \Omega_0)$ is provided. More importantly, there will be no closure issues when Eq. (5) is employed for the estimation of $\alpha_{\mathrm{w}}(\lambda)$ via Eq. (2). This new scheme is hereafter referred to as Chl-α_{w}_new.

3. Data and methods

3.1. Simulated datasets by HydroLight

Since field measurement of $\alpha_{\mathrm{w}}(\lambda)$ is not yet possible due to difficulties in separating the surface-reflected irradiance from the total upwelling irradiance [26], numerical simulations of radiative transfer by HydroLight code [27] are used in this study for the evaluation of Chl-α_{w}_new. HydroLight was selected because it can provide the angular distribution of $L_{\mathrm{w}}(\lambda)$ and thus the computation of 'true' $\alpha_{\mathrm{w}}(\lambda)$. Detailed descriptions of the configurations of HydroLight simulation can be found in Section 2.2 of Yu et al. [28]. Briefly, three simulated datasets were generated by HydroLight to evaluate the sensitivity of Chl-α_{w}_new to particle scattering phase function, Raman scattering, and chlorophyll fluorescence. The water was assumed homogenous and optically deep, whereas the default atmospheric models in HydroLight to characterize the sky radiances and irradiances distribution were employed with the assumption of zero cloud coverage (clear sky).

The first dataset, termed *SynData*, was generated with 500 sets of IOPs representing clear to turbid waters, three sets of wind speeds (5, 10, and 15 m/s), eight options of θ_{s} (0°, 15°, 30°, 45°, 60°, 75°, 80°, and 88°), and the Petzold average particle scattering phase function with an effective particulate backscattering-to-scattering ratio (b_{bpr}) of 1.83% [29]. The simulated $R_{\mathrm{rs}}(\lambda)$ and $\alpha_{\mathrm{w}}(\lambda)$ cover a spectral domain of 400–750 nm with an interval of 10 nm. Note that inelastic scattering, including Raman scattering and chlorophyll fluorescence, were not considered in *SynData*. The second dataset, termed *SynData*-FF, was generated following the same configuration as that in *SynData*, except that the particle scattering phase function was modeled by the Fournier-Forand model with an effective b_{bpr} of 1% [30]. The third dataset, termed *SynData*-RF, was simulated with Petzold average particle scattering phase function but with considerations of both Raman scattering and chlorophyll fluorescence, where the fluorescent quantum efficiency was set to 0.020.

3.2. Satellite imagery

The level-3 monthly composite global $R_{\mathrm{rs}}(\lambda)$ product of VIIRS, at a spatial resolution of 9 km, was acquired from NOAA CoastWatch (https://coastwatch.noaa.gov) and was used in this study to evaluate the performance of different α_{w} schemes. Here VIIRS monthly composite $R_{\mathrm{rs}}(\lambda)$ of March 2019 was downloaded for demonstration. Note that using a different VIIRS imagery will not change the results and conclusion of this effort.

3.3. Broadband albedo

In addition to the estimated spectral $\alpha_{\mathrm{w}}(\lambda)$ from multiple schemes, evaluation results of the broadband α_{w} in the visible domain ($\alpha_{\mathrm{w\_VIS}}$) are also provided. For hyperspectral $\alpha_{\mathrm{w}}(\lambda)$, $\alpha_{\mathrm{w\_VIS}}$ is calculated as the integral of $\alpha_{\mathrm{w}}(\lambda)$, weighted by $E_{\mathrm{d}}(0^{+}, \lambda)$, between 400 and 700 nm [31], which can be expressed as

$$\alpha_{\mathrm{w\_VIS}} = \frac{\int_{400}^{700} \alpha_{\mathrm{w}}(\lambda) E_{\mathrm{d}}(0^{+}, \lambda)}{\int_{400}^{700} E_{\mathrm{d}}(0^{+}, \lambda)}. \tag{6}$$

For multi-bands $\alpha_{\mathrm{w}}(\lambda)$ derived from ocean color measurements, $\alpha_{\mathrm{w\_VIS}}$ can be calculated following

$$\alpha_{\mathrm{w\_VIS}} = \sum_{i=1}^{5} k_i \alpha_{\mathrm{w}}(\lambda_i) + k_0, \tag{7}$$

where $\alpha_{\mathrm{w}}(\lambda_i)$ are the derived $\alpha_{\mathrm{w}}(\lambda)$ at the five visible VIIRS bands centered at 410, 443, 486, 551, and 671 nm, respectively. k_i ($i = 1$–5) are the narrowband-to-broadband conversion coefficients for the corresponding VIIRS bands and k_0 is a constant. The values of k_{0-5} can be retrieved from Table 1 of Yu et al. [28] for the VIIRS band configuration.

Table 1. The MRPD of estimated $\alpha_{\mathrm{w}}(\lambda)$ and $\alpha_{\mathrm{w\_VIS}}$ by Chl-α_{w}_new and IOPs-α_{w} for evaluation results using *SynData, SynData*-FF, *and SynData*-RF, respectively.

MRPD (%)	*SynData*		*SynData*-FF		*SynData*-RF	
	Chl-α_{w}_new	IOPs-α_{w}	Chl-α_{w}_new	IOPs-α_{w}	Chl-α_{w}_new	IOPs-α_{w}
410 nm	−2.1	2.0	−1.1	1.5	−2.0	2.6
440 nm	−0.9	1.8	−0.3	1.4	−1.1	2.5
490 nm	1.6	1.1	1.6	0.9	1.1	1.7
550 nm	3.4	2.0	2.6	1.2	2.3	3.2
670 nm	−0.3	7.1	−0.3	5.9	0.8	10.5
$\alpha_{\mathrm{w\_VIS}}$	1.7	1.5	1.6	1.2	1.1	2.3

3.4. IOPs-based scheme for α_w

For proper comparison, a recently-developed α_{w} scheme based on remotely sensed IOPs is also employed in this study for scheme inter-comparison [28]. The scheme based on IOPs, hereafter termed IOPs-α_{w}, ensures the closure of $R_{\mathrm{rs}}(\lambda)$ but employs a different model to describe the bidirectional variation of angular $R_{\mathrm{rs}}(\lambda)$ [32], which is expressed as

$$R_{\mathrm{rs}}(\lambda, \Omega) = \left(G_0^{w}(\Omega) + G_1^{w}(\Omega) \frac{b_{bw}(\lambda)}{\kappa(\lambda)} \right) \frac{b_{bw}(\lambda)}{\kappa(\lambda)} + \left(G_0^{p}(\Omega) + G_1^{p}(\Omega) \frac{b_{bp}(\lambda)}{\kappa(\lambda)} \right) \frac{b_{bp}(\lambda)}{\kappa(\lambda)}, \tag{8}$$

where $b_{bw}(\lambda)$ and $b_{bp}(\lambda)$ are the backscattering coefficients of pure seawater and particles, respectively. $\kappa(\lambda)$ is the sum of $a(\lambda)$ and $b_b(\lambda)$. $b_{bw}(\lambda)$ is considered known, while $b_{bp}(\lambda)$ and $a(\lambda)$ are derived from satellite-measured $R_{\mathrm{rs}}(\lambda)$ using the quasi-analytic algorithm [32,33], which ensures the closure of $R_{\mathrm{rs}}(\lambda)$ (see the detailed descriptions of IOPs inversion in Yu et al. [28]). $\mathrm{G}_0^{\mathrm{w}}(\Omega)$, $\mathrm{G}_1^{\mathrm{w}}(\Omega)$, $\mathrm{G}_0^{\mathrm{p}}(\Omega)$, and $\mathrm{G}_1^{\mathrm{p}}(\Omega)$ are model coefficients that can be retrieved from a look-up-table (LUT) for given angular geometry [28].

Note that Wei et al. [34] also employed Eq. (8) to model the angular $R_{\mathrm{rs}}(\lambda, \Omega)$ but with $b_{bp}(\lambda)$ and $a(\lambda)$ inferred from Chl using the Chl-IOPs relationship of Morel and Maritorena [14]. Thus, the scheme proposed by Wei et al. [34] cannot guarantee the closure of $R_{\mathrm{rs}}(\lambda)$ and can be considered a variant of the Chl-based scheme.

Optics EXPRESS

4. Results and discussions

4.1. Evaluation of Chl-α_w_new with numerical simulations

The performance of Chl-$\alpha_{\rm w}$, Chl-$\alpha_{\rm w}$_new, and IOPs-$\alpha_{\rm w}$ are first evaluated with *SynData*, with validation results of $\alpha_{\rm w}(\lambda)$ and $\alpha_{\rm w\_VIS}$ estimated by the three schemes presented in Fig. 2. The median RPD (MRPD) of estimated $\alpha_{\rm w}(\lambda)$ and $\alpha_{\rm w\_VIS}$ are also provided in Fig. 2 as a quantitative measure. Here RPD is first calculated using Eq. (4) with x as the estimated $\alpha_{\rm w}(\lambda)$ and y as the known $\alpha_{\rm w}(\lambda)$ from HydroLight simulations. MRPD is subsequently calculated as the median value of computed RPD of all simulations. Note that both the estimated $\alpha_{\rm w\_VIS}$ and known $\alpha_{\rm w\_VIS}$ are computed from the hyperspectral $\alpha_{\rm w}(\lambda)$ using Eq. (6). As shown in Fig. 2, for the simulated dataset *SynData*, Chl-$\alpha_{\rm w}$_new outperforms Chl-$\alpha_{\rm w}$ with much smaller errors in the estimated $\alpha_{\rm w}(\lambda)$ at all wavelengths. The absolute values of MRPD of estimated $\alpha_{\rm w}(\lambda)$ by Chl-$\alpha_{\rm w}$_new are generally less than 3.4% in comparison to over 32% for that by Chl-$\alpha_{\rm w}$. The systematic underestimations of $\alpha_{\rm w}(\lambda)$ by Chl-$\alpha_{\rm w}$ are due to the modeled $R_{\rm rs}(\lambda)$ from Chl-inferred IOPs are overall smaller than the input $R_{\rm rs}(\lambda)$ (see Fig. 1), resulting in negative MRPD at all spectral bands. Since both Chl-$\alpha_{\rm w}$_new and IOPs-$\alpha_{\rm w}$ are exempt from the errors associated with the closure issue of $R_{\rm rs}(\lambda)$, the uncertainties in estimated $\alpha_{\rm w}(\lambda)$ by these two schemes are mainly attributed to the respective model for the bidirectional variation of angular $R_{\rm rs}(\lambda)$, which are acceptable given the small values in MRPD. Figure 2 shows that Chl-$\alpha_{\rm w}$_new has quite comparable performance with IOPs-$\alpha_{\rm w}$ at all spectral bands, with all their retrievals closely distributed along the 1:1 line. In particular, the MRPD of estimated $\alpha_{\rm w\_VIS}$ by Chl-$\alpha_{\rm w}$_new and IOPs-$\alpha_{\rm w}$ are 1.7% and 1.5%, respectively. The difference in MRPD is only 0.2%, which is not statistically significant. Thus, Chl-$\alpha_{\rm w}$_new can be considered an alternative to IOPs-$\alpha_{\rm w}$ to accurately estimate $\alpha_{\rm w}(\lambda)$ from remote sensing, but much easier in calculations as it does not require the step to obtain IOPs.

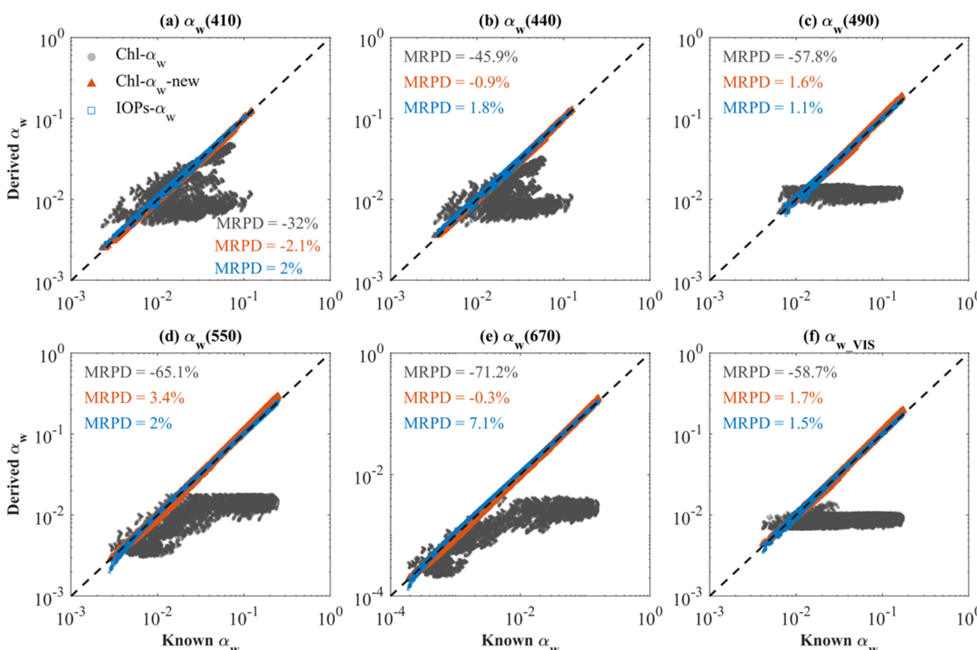

Fig. 2. Validation of estimated $\alpha_{\rm w}(\lambda)$ at five VIIRS bands and estimated $\alpha_{\rm w\_VIS}$ by Chl-$\alpha_{\rm w}$ (circles), Chl-$\alpha_{\rm w}$-new (triangles), and IOPs-$\alpha_{\rm w}$ (squares) using *SynData*.

Chl-$\alpha_{\rm w}$_new was further employed to estimate $\alpha_{\rm w}(\lambda)$ using *SynData*-FF and *SynData*-RF to evaluate the sensitivity of Chl-$\alpha_{\rm w}$_new to the particle scattering phase function, Raman scattering, and chlorophyll fluorescence, with the statistical measure tabulated in Table 1. Note that results from IOPs-$\alpha_{\rm w}$ are also included in Table 1 for comparisons, while results from Chl-$\alpha_{\rm w}$ are not shown here given its poor performance. It can be found in Table 1 that the absolute MRPD values are generally less than 3% for estimated $\alpha_{\rm w}(\lambda)$ and $\alpha_{\rm w\_VIS}$ by Chl-$\alpha_{\rm w}$_new for *SynData*-FF and *SynData*-RF, which are quite comparable with that obtained in *SynData*. Thus, we can conclude that Chl-$\alpha_{\rm w}$_new is insensitive to the particle scattering phase function, Raman scattering, and chlorophyll fluorescence, and could be applicable for the estimation of $\alpha_{\rm w}(\lambda)$ in a wide range of water types. Note that the evaluation results regarding the sensitivity of Chl-$\alpha_{\rm w}$_new to wind speed are not shown here as wind speed has negligible impacts on the estimated $\alpha_{\rm w}(\lambda)$ by Chl-$\alpha_{\rm w}$_new. Different wind speeds may alter the value of $\Re$ (Ω), but such an impact is largely canceled out when the ratio of $\Re$ (Ω) to $\Re$ (Ω_0) is used to model the angular $R_{\rm rs}(\lambda)$ (see Eq. (5)).

Furthermore, comparisons between Chl-$\alpha_{\rm w}$_new and IOPs-$\alpha_{\rm w}$ in Table 1 show that Chl-$\alpha_{\rm w}$_new has slightly degraded performance compared to IOPs-$\alpha_{\rm w}$ in *SynData*-FF, but their difference is overall comparable. However, for *SynData*-RF, Chl-$\alpha_{\rm w}$_new has shown improved performance than IOPs-$\alpha_{\rm w}$ with a much smaller MRPD of estimated $\alpha_{\rm w\_VIS}$. Thus, Chl-$\alpha_{\rm w}$_new would be highly recommended for applications in eutrophic waters where chlorophyll fluorescence could be significant.

4.2. *Evaluation of Chl-α_w_new with satellite imagery*

VIIRS imagery is further employed to evaluate the performance of Chl-$\alpha_{\rm w}$_new in the global ocean, especially for its comparison with Chl-$\alpha_{\rm w}$ and IOPs-$\alpha_{\rm w}$. Here, VIIRS monthly composite $R_{\rm rs}(\lambda)$ of March 2019 are employed to estimate $\alpha_{\rm w}(\lambda)$ for the subsequent demonstration and analysis. Other inputs required for Chl-$\alpha_{\rm w}$ and Chl-$\alpha_{\rm w}$_new are the solar zenith angle and wind speed, with $\theta_{\rm s}$ set as 0 given the fact that VIIRS $R_{\rm rs}(\lambda)$ product is equivalent to $R_{\rm rs}(\lambda,0,0,0)$. Note that wind speed has rather minor impact on $\alpha_{\rm w}(\lambda)$ [28], thus a constant 6.64 m/s is used for all pixels, which is the global average wind speed at 10 m above the ocean [35]. The extra input required for the implementation of IOPs-$\alpha_{\rm w}$ is $\theta_{\rm s}$, which is also set as 0.

The differences between estimated $\alpha_{\rm w}(\lambda)$ by Chl-$\alpha_{\rm w}$ and its improved version Chl-$\alpha_{\rm w}$_new in global oceans are first evaluated for all the five VIIRS visible bands with results presented in Fig. 3. RPD is calculated following Eq. (4) with estimated $\alpha_{\rm w}(\lambda)$ by Chl-$\alpha_{\rm w}$ as the reference (*i.e.*, the denominator in Eq. (4)). Comparisons of spectral $\alpha_{\rm w}(\lambda)$ estimated by Chl-$\alpha_{\rm w}$_new and IOPs-$\alpha_{\rm w}$ for global oceans are not shown here as they are very comparable. As shown in Fig. 3, for most oceanic waters, Chl-$\alpha_{\rm w}$ systematically underestimates $\alpha_{\rm w}(\lambda)$ at the five VIIRS bands, except for waters in the North Atlantic Ocean and the North Pacific Ocean. In most coastal regions, Chl-$\alpha_{\rm w}$ tends to overestimate $\alpha_{\rm w}(\lambda)$ except for those with high turbidity or shallow depths.

Further, we select three regions of interest (ROIs, highlighted in Fig. 3(d)) to highlight the different $\alpha_{\rm w}(\lambda)$ obtained by Chl-$\alpha_{\rm w}$, Chl-$\alpha_{\rm w}$_new, and IOPs-$\alpha_{\rm w}$ in different types of waters. These three ROIs are the North Atlantic Ocean (NAO, 55°W – 45°W, 43°N – 47°N), the South Pacific Gyre (SPG, 124°W – 104°W, 32°S – 22°S), and the Yangtze estuary (YE, 120.7°E – 123.0°E, 29.5°N – 32.5°N), which are selected because NAO represents oceanic waters where Chl-$\alpha_{\rm w}$_new yields significantly smaller $\alpha_{\rm w}(\lambda)$ than Chl-$\alpha_{\rm w}$, while SPG is for oceanic waters with larger $\alpha_{\rm w}(\lambda)$ estimations by Chl-$\alpha_{\rm w}$_new. YE is selected due to it is characteristics of extremely turbid waters [36]. The bio-optical properties (Chl and IOPs) are also derived from $R_{\rm rs}(\lambda)$ to highlight the contrasting water characteristics in these three ROIs. Specifically, Chl is estimated by the OCI algorithm [15–17], while a and b_b are derived using the quasi-analytical algorithm (QAA) [33]. Note that the latest version of QAA (QAA_v6, available at http://www.ioccg.org/groups/Software_OCA/QAA_v6_2014209.pdf) was used in this study. In Fig. 4, we present the median spectra of derived $\alpha_{\rm w}(\lambda)$ by the three schemes in the three ROIs, as well as the spectra of VIIRS-measured $R_{\rm rs}(\lambda)$ and the modeled $R_{\rm rs}(\lambda)$ from Chl-inferred IOPs.

Optics EXPRESS

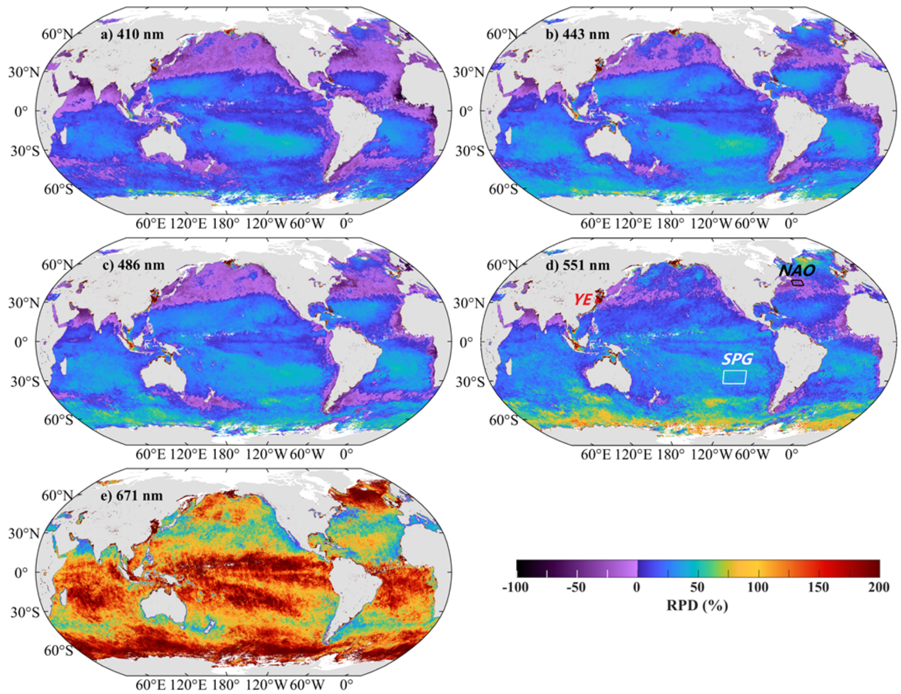

Fig. 3. Same as Fig. 1, but for RPD of the estimated $\alpha_w(\lambda)$ by Chl-α_w_new, referring to that by Chl-α_w. The black, white, and red boxes in panel (d) highlight the locations of three regions of interest in the North Atlantic Ocean (NAO), South Pacific Gyre (SPG), and Yangtze estuary, respectively.

It can be observed in Fig. 4 that, for all three ROIs, the estimated $\alpha_w(\lambda)$ by Chl-α_w is significantly deviated from that by Chl-α_w_new and IOPs-α_w. As a quantitative measure, Table 2 tabulates the median RPD of the estimated $\alpha_w(\lambda)$ by Chl-α_w_new, referring to the estimation by Chl-α_w, for the three ROIs, as well as the median RPD of VIIRS $R_{rs}(\lambda)$, referring to the modeled $R_{rs}(\lambda)$. It can be found that Chl-α_w_new, on average, predicts much smaller $\alpha_w(\lambda)$ in NAO than that by Chl-α_w, with MRPD generally less than −20% in the blue-green domain. For SPG and YE, estimated $\alpha_w(\lambda)$ by Chl-α_w_new are significantly greater than that by Chl-α_w, especially for the YE where MRPD could be over 2000%. As shown in Table 2, the MRPD values calculated for VIIRS $R_{rs}(\lambda)$, referring to the modeled $R_{rs}(\lambda)$ by Chl-α_w, are very comparable with the MRPD for estimated spectral $\alpha_w(\lambda)$ (see also the comparison of Fig. 1 and Fig. 3), suggesting that the large discrepancies of estimated $\alpha_w(\lambda)$ between Chl-α_w_new and Chl-α_w could be mainly attributed to the uncertainties introduced by the modeling of angular $R_{rs}(\lambda)$ from Chl-inferred IOPs. Thus, it is safe to conclude that Chl-α_w_new provides a more reasonable estimation of $\alpha_w(\lambda)$ than Chl-α_w in global oceans, given that it avoids the uncertainties associated with the closure issue of $R_{rs}(\lambda)$.

Consistent with the results presented in Table 1 for the evaluation results with *SynData*, Chl-α_w_new and IOPs-α_w have quite comparable performance when implemented to VIIRS data, where the spectral $\alpha_w(\lambda)$ estimated by both schemes are almost congruent in the three ROIs, especially in NAO and SPG (see Fig. 4(a) and Fig. 4(b)). Discrepancies in the estimated $\alpha_w(\lambda)$ are observed in the YE but are statistically insignificant (see Fig. 4(c)). Table 3 tabulates the MRPD between estimated $\alpha_w(\lambda)$ by Chl-α_w_new and IOPs-α_w, with estimations by IOPs-α_w as the reference, where MRPD are found within ± 5% for most spectral bands for all three ROIs, suggesting a good agreement between Chl-α_w_new and IOPs-α_w. More importantly,

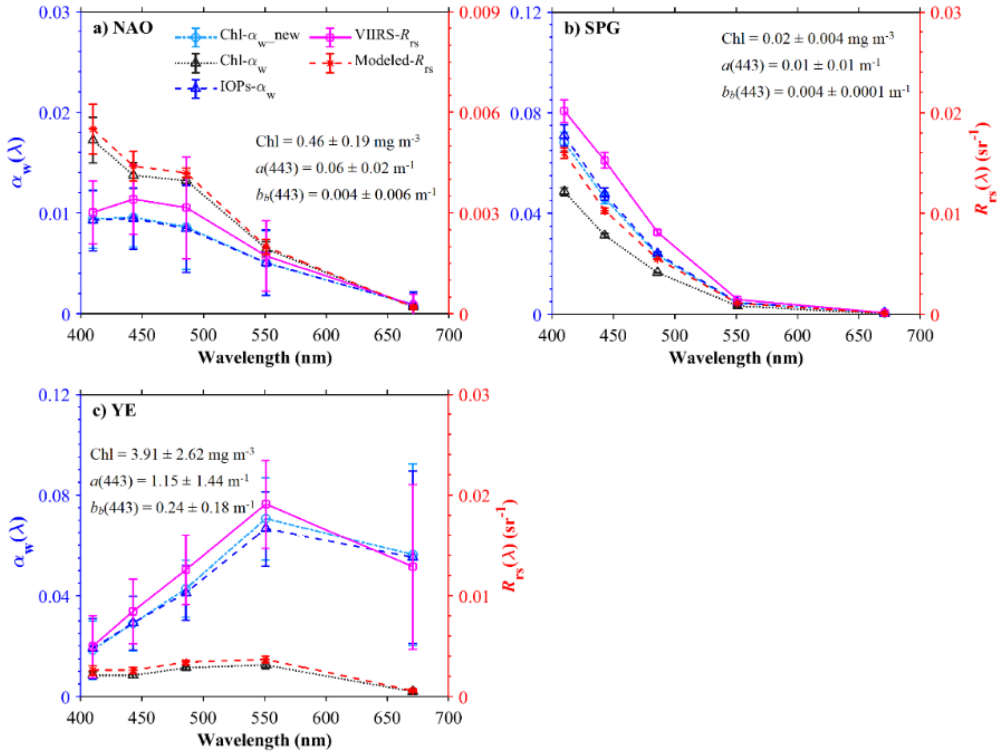

Fig. 4. Comparisons of the estimated spectral $\alpha_{\mathrm{w}}(\lambda)$ (aligned to the left y-axis) by Chl-α_{w}_new, Chl-α_{w}, and IOPs-α_{w}, and comparisons of the spectral $R_{\mathrm{rs}}(\lambda)$ (aligned to the right y-axis) from VIIRS measurements and that modeled from Chl-inferred IOPs, for NAO, SPG, and YE, respectively. The median values (med) of $\alpha_{\mathrm{w}}(\lambda)$ and $R_{\mathrm{rs}}(\lambda)$ are plotted here, with the error bar indicating the standard deviation (std). Remotely sensed Chl, $a(443)$, and $b_b(443)$ (med ± std) are also presented to highlight the distinguishing characteristics of water properties in the three ROIs.

Table 2. The MRPD of estimated $\alpha_{\mathrm{w}}(\lambda)$ by Chl-α_{w}_new, referring to that estimated by Chl-α_{w}, and the MRPD of VIIRS $R_{\mathrm{rs}}(\lambda)$, referring to that modeled from Chl, for the three regions of interest in NAO, SPG, and YE, respectively.

MRPD (%)	$\alpha_{\mathrm{w}}(\lambda)$			$R_{\mathrm{rs}}(\lambda)$		
	NAO	SPG	YE	NAO	SPG	YE
410 nm	−45.4	40.1	118.8	−45.0	26.0	90.9
443 nm	−30.2	47.9	245.8	−22.5	48.2	225.5
486 nm	−34.9	42.0	276.7	−24.8	48.3	270.2
551 nm	−21.3	37.5	464.4	−13.7	33.8	415.8
671 nm	31.9	145.5	2744.4	28.7	47.2	2047.1

the differences between the estimated $\alpha_{\mathrm{w\_VIS}}$ by the two schemes in the three ROIs are even smaller, with MRPD of 0.2%, −3.6%, and 2.9% for NAO, SPG, and YE, respectively. Thus, evaluation results with satellite imagery also suggest that Chl-α_{w}_new is a good alternative to IOPs-α_{w}. Here $\alpha_{\mathrm{w\_VIS}}$ is converted from the narrowband $\alpha_{\mathrm{w}}(\lambda)$ following Eq. (7). As shown in Table 3, although there are small discrepancies in the spectral $\alpha_{\mathrm{w}}(\lambda)$ estimated by Chl-α_{w}_new and IOPs-α_{w}, estimated $\alpha_{\mathrm{w\_VIS}}$ by the two schemes are quite consistent with the absolute MRPD less than 4% at all the three ROIs.

Table 3. The Median RPD (MRPD) of estimated $\alpha_{\mathrm{w}}(\lambda)$ and $\alpha_{\mathrm{w\_VIS}}$ by Chl-α_{w}_new, referring to that estimated by IOPs-α_{w}, for the three regions of interest in NAO, SPG, and YE, respectively.

MRPD (%)	NAO	SPG	YE
$\alpha_{\mathrm{w}}(410)$	1.3	−3.8	−3.6
$\alpha_{\mathrm{w}}(443)$	1.3	−3.4	−0.3
$\alpha_{\mathrm{w}}(486)$	1.8	−2.9	3.8
$\alpha_{\mathrm{w}}(551)$	0.1	−5.1	6.1
$\alpha_{\mathrm{w}}(671)$	−4.2	−8.5	1.8
$\alpha_{\mathrm{w\_VIS}}$	0.2	−3.6	2.9

In Fig. 5(a), we show the global distribution of $\alpha_{\mathrm{w\_VIS}}$ estimated by Chl-α_{w}_new using the VIIRS monthly composite data of March 2019. The differences between estimated $\alpha_{\mathrm{w\_VIS}}$ by Chl-α_{w}_new and IOPs-α_{w} in global oceans are demonstrated in Fig. 5(c), with the comparison of Chl-α_{w} and IOPs-α_{w} shown in Fig. 5(b). Results in Fig. 5(c) confirm that Chl-α_{w}_new could be equivalent to IOPs-α_{w} for the estimation of $\alpha_{\mathrm{w\_VIS}}$, as the differences in estimated $\alpha_{\mathrm{w\_VIS}}$ by the two schemes in the global ocean are generally less than 5%. In contrast, the median RPD values for the three ROIs calculated from Fig. 5(b) are 39.9%, −33.0%, and −86.5%, respectively, suggesting that both Chl-α_{w}_new and IOPs-α_{w} can significantly improve the estimation of $\alpha_{\mathrm{w\_VIS}}$ compared to Chl-α_{w}, especially for turbid waters.

4.3. Uncertainties in different α_w schemes

Since Chl-α_{w} and Chl-α_{w}_new employ the same model to describe the bidirectional variation of $R_{\mathrm{rs}}(\lambda)$, comparisons between these two schemes conclude that optical closure of $R_{\mathrm{rs}}(\lambda)$ is the main error source for estimated $\alpha_{\mathrm{w}}(\lambda)$ by Chl-α_{w}. The underestimation or overestimation of $\alpha_{\mathrm{w}}(\lambda)$ by Chl-α_{w} in the global ocean is driven largely by the extent of underestimation or overestimation in modeled $R_{\mathrm{rs}}(\lambda)$ from Chl, which is determined by the uncertainties in the Chl-inferred IOPs, particularly the ratio of $b_b(\lambda)$ to $a(\lambda)$. Since the Chl-IOPs relationship used in Chl-α_{w} was proposed for "Case-1" waters [14], it is not surprising that larger uncertainties of estimated $\alpha_{\mathrm{w}}(\lambda)$ by Chl-α_{w} are found in most coastal waters, which are typically more optically complex and IOPs are not solely determined by Chl [37]. However, for oceanic waters, Chl-α_{w} is still underperformed and its performance is region-dependent (see Fig. 3), which can be explained by the uncertainties in Chl-inferred IOPs in different regions.

For instance, the overestimation of $\alpha_{\mathrm{w}}(\lambda)$ by Chl-α_{w} in NAO could be mainly due to underestimated absorption coefficient of colored dissolved organic matter (CDOM), termed $a_g(\lambda)$ hereafter. Comparing with Fig. 1(b) of Morel et al. [38], we can observe that the purple to black pixels in Fig. 3 are highly coincident with waters of high CDOM-to-Chl proportion. Chl-α_{w} uses an empirical relationship to estimate $a_g(\lambda)$ from Chl [14] could result in large uncertainties in estimated $a_g(\lambda)$ when applying the relationship to global oceans, especially for waters where the CDOM-to-Chl proportion differs largely from these statistical averages. For those waters with a high CDOM-to-Chl proportion, the empirical Chl-$a_g(\lambda)$ relationship used by Chl-α_{w} would

Optics EXPRESS

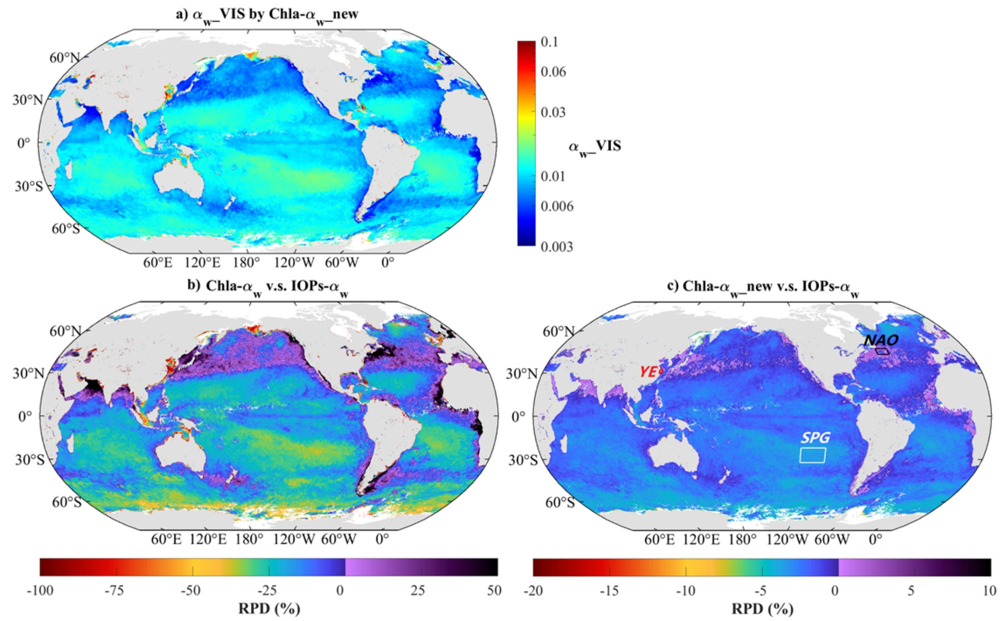

Fig. 5. Global distribution of α_{w_VIS} in March 2019 estimated by Chl-α_w_new using VIIRS monthly composite data (a). Panels (b) and (c) show the RPD of estimated α_{w_VIS} by Chl-α_w and Chl-α_w_new, referring to α_{w_VIS} estimated by IOPs-α_w, respectively (note the difference in the scale of the colorbar in panels (b) and (c)).

underestimate $a(\lambda)$, which results in larger modeled $R_{rs}(\lambda)$, and hence an overestimation of $\alpha_w(\lambda)$ (see Fig. 4(a)).

For waters in SPG and other oceanic waters where Chl-α_w underestimates $\alpha_w(\lambda)$, the underestimations of the modeled $R_{rs}(\lambda)$ are mostly attributed to the underestimated $b_b(\lambda)$ from Chl. For example, Chl-inferred $a(\lambda)$ in SPG are overall comparable with the derived $a(\lambda)$ from VIIRS $R_{rs}(\lambda)$ using QAA_v6, but Chl-inferred $b_b(\lambda)$ are underestimated by more than 30% at the five bands (results not shown here). Consequently, the underestimations of $b_b(\lambda)$ result in smaller modeled $R_{rs}(\lambda)$ in SPG, which explains the biased lower $\alpha_w(\lambda)$ estimation by Chl-α_w (see Table 2). For YE, Chl-inferred $a(\lambda)$ and $b_b(\lambda)$ are both of large uncertainties, but underestimation of $b_b(\lambda)$ prevails over the underestimation of $a(\lambda)$ given that the waters in YE are extremely turbid and are characteristics of strong backscattering. Thus, modeled $R_{rs}(\lambda)$ from Chl in YE are significantly underestimated, hence the estimated $\alpha_w(\lambda)$ (see Fig. 4(c)).

On the other hand, both Chl-α_w_new and IOPs-α_w avoid the uncertainties associated with the closure issue of $R_{rs}(\lambda)$, while their differences lie in the models for bidirectional variation of $R_{rs}(\lambda)$. Comparisons of Chl-α_w_new and IOPs-α_w for their performance in both HydroLight simulations and VIIRS data show that the model for $R_{rs}(\lambda)$ bidirectionality has rather minor impacts on the uncertainties in the estimated $\alpha_w(\lambda)$. It is worthy to point out that the uncertainties of derived Chl from OCI could be considerably large in optically complex waters [39–41], which will introduce errors to modeled angular $R_{rs}(\lambda)$ as the values of Ψ in Eq. (3) is Chl-dependent. However, it is found that the ratios of $\Psi(\Omega)$ to $\Psi(\Omega_0)$ are in a much smaller range than the range of the Ψ values [20]. Thus, Chl-α_w_new could be less sensitive to the uncertainties in the Ψ values associated with the use of empirically estimated Chl, which can explain the consistent performance of Chl-α_w_new in the extremely turbid waters in YE as presented in Fig. 4(c). It is also noted that the LUT to describe $R_{rs}(\lambda)$ bidirectionality in IOPs-α_w, *i.e.*, the G values in Eq. (8), is weighted for all wavelengths and could result in uncertainties in modeled angular

Optics EXPRESS

$R_{\mathrm{rs}}(\lambda)$ for a specific wavelength, especially for the red domain [28]. In contrast, the LUT for Ψ is wavelength-dependent, which might explain the result that Chl-α_{w}_new outperforms IOPs-α_{w} for the estimated $\alpha_{\mathrm{w}}(670)$ as shown in Table 1. This suggests that IOPs-α_{w} might be further improved if the LUT for G values is wavelength-dependent.

4.4. Implications for coupled ocean-atmosphere models

Since both Chl-α_{w}_new and IOPs-α_{w} could significantly improve the estimation of $\alpha_{\mathrm{w}}(\lambda)$ compared to the conventional Chl-α_{w}, the remaining question would be how much the improvement could affect the interpretation of solar radiation transfer at the air-sea boundary layer in coupled ocean-atmosphere models and climate models. Many previous studies considered only the reflected albedo in their parametrizations of the ocean surface albedo ($\alpha(\lambda)$) or simply use a constant broadband α value for global oceans [42]. The broadband α, termed α_{broad}, is calculated as the integral of spectral $\alpha(\lambda)$ over the full shortwave domain and weighted by $E_{\mathrm{d}}(0^{+}, \lambda)$ [31]. Some recent efforts included the contribution of $\alpha_{\mathrm{w}}(\lambda)$ to $\alpha(\lambda)$ but the contribution of $\alpha_{\mathrm{w}}(\lambda)$ might be largely underrepresented as they employed Chl-α_{w} [9–11]. Given that the reflected albedo is generally less than 0.03 for solar zenith angles less than 30° (see Fig. 15 in Feng et al. [10]), we can preliminarily assess the contribution of $\alpha_{\mathrm{w}}(\lambda)$ to α_{broad} as the broadband α_{w} (termed $\alpha_{\mathrm{w\_broad}}$) is about 42.3% of $\alpha_{\mathrm{w\_VIS}}$ if neglecting the contribution of $\alpha_{\mathrm{w}}(\lambda)$ from ultraviolet and near-infrared bands [28]. The selection of the value of 42.3% is simply because $E_{\mathrm{d}}(0^{+}, \lambda)$ in the visible domain accounts for roughly 42.3% of $E_{\mathrm{d}}(0^{+}, \lambda)$ in the full shortwave domain [43]. Such an assumption is valid for most of the global oceans except for extremely turbid waters, where $\alpha_{\mathrm{w\_broad}}$ could be much larger than 42.3% of $\alpha_{\mathrm{w\_VIS}}$ due to contributions from $\alpha_{\mathrm{w}}(\lambda)$ of near-infrared bands.

Take the SPG for example, the median $\alpha_{\mathrm{w\_VIS}}$ estimated by Chl-α_{w}_new and Chl-α_{w} are 0.017 and 0.011, respectively, resulting in the median $\alpha_{\mathrm{w\_broad}}$ of 0.0072 and 0.0046 when multiplying $\alpha_{\mathrm{w\_VIS}}$ by 42.3%. Taking the reflected albedo as a constant of 0.03, α_{broad} would increase from 0.0346 to 0.0372 if Chl-α_{w}_new is employed. Such a change in α_{broad} would have minimal impacts ($\sim -0.4\%$) on the calculation of solar radiation absorbed by the ocean, which is a function of $1 - \alpha_{\mathrm{broad}}$ (*i.e.*, 0.965 vs 0.963). However, the amount of reflected flux towards the atmosphere would be increased by 7.5% in this case, which could be important for the energy budget given gyre waters account for over 30% of surface areas of the global oceans. Furthermore, if applying the same calculation scheme to YE, the median α_{broad} estimated by Chl-α_{w} and Chl-α_{w}_new would be 0.0335 to 0.0565, respectively, which means the solar radiation absorbed by the ocean would decrease by 2.4% if Chl-α_{w}_new is employed, while the reflected solar energy towards the atmosphere will surge by 68.7%. Note that if the contribution of $\alpha_{\mathrm{w}}(\lambda)$ from near-infrared bands is taken into consideration, a larger α_{broad} in YE would be expected, which means more solar radiation will be reflected into the atmosphere at the air-sea interface.

The preliminary assessment discussed above highlights the fact that $\alpha_{\mathrm{w}}(\lambda)$ contribution to α_{broad} should not be neglected in the coupled ocean-atmosphere models, especially for the models requiring the reflected solar flux at the air-sea interface and models for solar radiation transfer in optically complex waters, such as the Regional Ocean Modeling System. It is highly recommended to implement either Chl-α_{w}_new or IOPs-α_{w} to the coupled ocean-atmosphere models and climate models for an accurate estimation of $\alpha_{\mathrm{w}}(\lambda)$. It can be expected that with more accurate inputs of $\alpha_{\mathrm{w}}(\lambda)$, the interpretation of solar radiation transfer at the air-sea boundary layer in these models and the feedback of ocean surface albedo to the climate change could be altered [44], particularly for the potential impacts on the air dynamics in the middle-to-low latitude oceans where the average solar zenith angles are relatively low and $\alpha_{\mathrm{w}}(\lambda)$ has high contributions to α_{broad}.

5. Conclusions

In this effort, we show that the conventional Chl-based α_w scheme could result in large uncertainties in the estimation of $\alpha_w(\lambda)$ for global oceans, which is mainly because of no closure between the modeled $R_{\rm rs}(\lambda)$ from Chl-inferred IOPs and the input $R_{\rm rs}(\lambda)$ for the retrieval of Chl. With a simple but analytical modification, we proposed a new scheme termed Chl-$\alpha_{\rm w}$_new, which skips the step to estimate IOPs from Chl, thus reducing the uncertainties in the estimated $\alpha_w(\lambda)$ greatly in global oceans. Comparisons between Chl-$\alpha_{\rm w}$_new and the IOPs-based scheme demonstrate that the closure of $R_{\rm rs}(\lambda)$ is the main error source for the estimation of $\alpha_w(\lambda)$ by Chl-based schemes, while the model for $R_{\rm rs}(\lambda)$ bidirectionality have rather minor impacts. Note that the field measurement system for $\alpha_w(\lambda)$ has already been proposed [26], further evaluations of the three $\alpha_w(\lambda)$ schemes could be carried out when field-measured $\alpha_w(\lambda)$ become available. Finally, this study highlights the necessity of incorporating accurate $\alpha_w(\lambda)$ in the coupled ocean-atmosphere models, especially for the estimation of reflected and scattered solar radiation towards the atmosphere at the air-sea interface.

Funding. National Natural Science Foundation of China (42006162, 41941008, 41890803); China Postdoctoral Science Foundation (2019M662234).

Acknowledgments. X. Yu is funded by the Outstanding Postdoctoral Scholarship of the State Key Laboratory of Marine Environmental Science at Xiamen University. The authors would like to thank Dr. Menghua Wang and Dr. Lide Jiang for providing the VIIRS data.

Disclosures. The authors declare no conflicts of interest.

Data availability. MATLAB scripts for both Chl-$\alpha_{\rm w}$ and Chl-$\alpha_{\rm w}$_new, as well as data underlying the results presented in this paper are available in Ref. [45].

References

1. J. P. Abraham, M. Baringer, N. Bindoff, T. Boyer, L. Cheng, J. Church, J. Conroy, C. Domingues, J. Fasullo, and J. Gilson, "A review of global ocean temperature observations: Implications for ocean heat content estimates and climate change," Rev. Geophys. **51**(3), 450–483 (2013).
2. R. E. Payne, "Albedo of the sea surface," J. Atmos. Sci. **29**(5), 959–970 (1972).
3. M. Fogarty, M. Fewings, A. Paget, and H. Dierssen, "The influence of a sandy substrate, seagrass, or highly turbid water on albedo and surface heat flux," J. Geophys. Res. Oceans **123**(1), 53–73 (2018).
4. Z. Jin, T. P. Charlock, W. L. Smith Jr, and K. Rutledge, "A parameterization of ocean surface albedo," Geophys. Res. Lett. **31**(22), L22301 (2004).
5. B. P. Briegleb, P. Minnis, V. Ramanathan, and E. Harrison, "Comparison of regional clear-sky albedos inferred from satellite observations and model computations," J. Climate Appl. Meteor. **25**(2), 214–226 (1986).
6. J. Taylor, J. Edwards, M. Glew, P. Hignett, and A. Slingo, "Studies with a flexible new radiation code. II: Comparisons with aircraft short-wave observations," Q. J. R. Meteorol. Soc. **122**(532), 839–861 (1996).
7. C. Cox and W. Munk, "Measurement of the roughness of the sea surface from photographs of the sun's glitter," J. Opt. Soc. Am. **44**(11), 838–850 (1954).
8. Z. Jin, T. P. Charlock, and K. Rutledge, "Analysis of broadband solar radiation and albedo over the ocean surface at COVE," J. Atmos. Oceanic Technol. **19**(10), 1585–1601 (2002).
9. R. Séférian, S. Baek, O. Boucher, J.-L. Dufresne, B. Decharme, D. Saint-Martin, and R. Roehrig, "An interactive ocean surface albedo scheme (OSAv1. 0): formulation and evaluation in ARPEGE-Climat (V6. 1) and LMDZ (V5A)," Geosci. Model Dev. **11**(1), 321–338 (2018).
10. Y. Feng, Q. Liu, Y. Qu, and S. Liang, "Estimation of the ocean water albedo from remote sensing and meteorological reanalysis data," IEEE Trans. Geosci. Remote Sens. **54**(2), 850–868 (2016).
11. Z. Jin, Y. Qiao, Y. Wang, Y. Fang, and W. Yi, "A new parameterization of spectral and broadband ocean surface albedo," Opt. Express **19**(27), 26429–26443 (2011).
12. C. D. Mobley, *Light and water: radiative transfer in natural waters* (Academic, 1994).
13. A. Morel and B. Gentili, "Diffuse reflectance of oceanic waters. II. Bidirectional aspects," Appl. Opt. **32**(33), 6864–6879 (1993).
14. A. Morel and S. Maritorena, "Bio-optical properties of oceanic waters: A reappraisal," J. Geophys. Res. **106**(C4), 7163–7180 (2001).
15. J. E. O'Reilly, S. Maritorena, B. G. Mitchell, D. A. Siegel, K. L. Carder, S. A. Garver, M. Kahru, and C. McClain, "Ocean color chlorophyll algorithms for SeaWiFS," J. Geophys. Res. **103**(C11), 24937–24953 (1998).
16. C. Hu, Z. Lee, and B. Franz, "Chlorophyll a algorithms for oligotrophic oceans: A novel approach based on three-band reflectance difference," J. Geophys. Res. **117**(C1), C01011 (2012).

Optics EXPRESS

17. M. Wang and S. Son, "VIIRS-derived chlorophyll-a using the ocean color index method," Remote Sens. Environ. **182**, 141–149 (2016).
18. H. R. Gordon, "Normalized water-leaving radiance: revisiting the influence of surface roughness," Appl. Opt. **44**(2), 241–248 (2005).
19. M. Wang, "Effects of ocean surface reflectance variation with solar elevation on normalized water-leaving radiance," Appl. Opt. **45**(17), 4122–4128 (2006).
20. A. Morel, D. Antoine, and B. Gentili, "Bidirectional reflectance of oceanic waters: accounting for Raman emission and varying particle scattering phase function," Appl. Opt. **41**(30), 6289–6306 (2002).
21. A. Bricaud, M. Babin, A. Morel, and H. Claustre, "Variability in the chlorophyll-specific absorption coefficients of natural phytoplankton: Analysis and parameterization," J. Geophys. Res. **100**(C7), 13321–13332 (1995).
22. H. Loisel and A. Morel, "Light scattering and chlorophyll concentration in case 1 waters: A reexamination," Limnol. Oceanogr. **43**(5), 847–858 (1998).
23. Y. Huot, A. Morel, M. Twardowski, D. Stramski, and R. Reynolds, "Particle optical backscattering along a chlorophyll gradient in the upper layer of the eastern South Pacific Ocean," Biogeosciences **5**(2), 495–507 (2008).
24. R. A. Reynolds, D. Stramski, and B. G. Mitchell, "A chlorophyll-dependent semianalytical reflectance model derived from field measurements of absorption and backscattering coefficients within the Southern Ocean," J. Geophys. Res. **106**(C4), 7125–7138 (2001).
25. M. Stramska, D. Stramski, R. Hapter, S. Kaczmarek, and J. Stoń, "Bio-optical relationships and ocean color algorithms for the north polar region of the Atlantic," J. Geophys. Res. Oceans, **108** (2003).
26. Z. Shang, X. Yu, and Z. Lee, "Direct measurement system of water-leaving albedo in the field by the skylight-blocked approach: Monte Carlo simulations," Opt. Express **30**(13), 23852–23867 (2022).
27. C. D. Mobley and L. K. Sundman, "*Hydrolight 5.3 Ecolight 5.3 Users' Guide*," Sequoia Scientific Inc. (2016).
28. X. Yu, Z. Lee, S. Shang, M. Wang, and L. Jiang, "Estimating the water-leaving albedo from ocean color," Remote Sens. Environ. **269**, 112807 (2022).
29. T. J. Petzold, "*Volume scattering functions for selected ocean waters*," (DTIC Document, 1972).
30. G. R. Fournier and J. L. Forand, "Analytic phase function for ocean water," in *Ocean Optics XII*, (International Society for Optics and Photonics, 1994), 194–201.
31. J. C. Ohlmann, D. A. Siegel, and C. D. Mobley, "Ocean radiant heating. Part I: Optical influences," J. Phys. Oceanogr. **30**(8), 1833–1848 (2000).
32. Z. P. Lee, K. Du, K. J. Voss, G. Zibordi, B. Lubac, R. Arnone, and A. Weidemann, "An inherent-optical-property-centered approach to correct the angular effects in water-leaving radiance," Appl. Opt. **50**(19), 3155–3167 (2011).
33. Z. Lee, K. L. Carder, and R. A. Arnone, "Deriving inherent optical properties from water color: a multiband quasi-analytical algorithm for optically deep waters," Appl. Opt. **41**(27), 5755–5772 (2002).
34. J. Wei, T. Ren, P. Yang, S. F. DiMarco, and E. Mlawer, "An improved ocean surface albedo computational scheme: Structure and Performance," J. Geophys. Res. Oceans, e2020JC016958 (2021).
35. C. L. Archer and M. Z. Jacobson, "Evaluation of global wind power," J. Geophys. Res. Atmos. 110(2005).
36. X. Yu, Z. Lee, F. Shen, M. Wang, J. Wei, L. Jiang, and Z. Shang, "An empirical algorithm to seamlessly retrieve the concentration of suspended particulate matter from water color across ocean to turbid river mouths," Remote Sens. Environ. **235**, 111491 (2019).
37. IOCCG, "Remote Sensing of Ocean Colour in Coastal, and Other Optically-Complex, Waters," Sathyendranath, S. (ed.), Reports of the International Ocean-Colour Coordinating Group No.3, IOCCG, Dartmouth, Canada (2000).
38. A. Morel, H. Claustre, and B. Gentili, "The most oligotrophic subtropical zones of the global ocean: similarities and differences in terms of chlorophyll and yellow substance," Biogeosciences **7**(10), 3139–3151 (2010).
39. G. F. Cota, H. Wang, and J. C. Comiso, "Transformation of global satellite chlorophyll retrievals with a regionally tuned algorithm," Remote Sens. Environ. **90**(3), 373–377 (2004).
40. S. Shang, Z. Lee, G. Lin, Y. Li, and X. Li, "Progressive scheme for blending empirical ocean color retrievals of absorption coefficient and chlorophyll concentration from open oceans to highly turbid waters," Appl. Opt. **58**(13), 3359–3369 (2019).
41. C. Le, C. Hu, J. Cannizzaro, D. English, F. Muller-Karger, and Z. Lee, "Evaluation of chlorophyll-a remote sensing algorithms for an optically complex estuary," Remote Sens. Environ. **129**, 75–89 (2013).
42. J. Li, J. Scinocca, M. Lazare, N. McFarlane, K. Von Salzen, and L. Solheim, "Ocean surface albedo and its impact on radiation balance in climate models," J. Clim. **19**(24), 6314–6333 (2006).
43. J. Gibson, "UVB radiation: definition and characteristics," USDA/CSU Available online: https://uvb.nrel.colostate.edu/UVB/publications/uvb_primer.pdf. (2003).
44. A. Hall, "The role of surface albedo feedback in climate," J. Clim. **17**(7), 1550–1568 (2004).
45. X. Yu, "MATLAB scripts for the new retrieval algorithm of water-leaving albedo based on Chlorophyll-a concentration", retrieved 9/3/2022, https://github.com/oceanopticsxmu/Chl_osaw. (Github, 2022).